Journal of Guidance, Control, and Dynamics
Vol. 38, No. 12, December 2015

Engineering Notes

Design of a Vibration Isolation System for the Space Telescope

Jianfeng Yang,* Zhenbang Xu,† Qingwen Wu,‡ Zhongsu Wang,§ Hang Li,¶ and Shuai He**
Changchun Institute of Optics, Fine Mechanics and Physics, Chinese Academy of Sciences, 130033 Changchun, People's Republic of China

DOI: 10.2514/1.G001221

I. Introduction

WITH the development of space technology, demands for a space telescope with a large aperture and high image resolution are increasing. The Hubble Space Telescope (HST), which was launched in 1990, can achieve a pointing stability of 0.007 arcsec over 24 h [1]. As the successor to the HST, the James Webb Space Telescope with a 6.5 m diameter, might achieve a pointing stability of 0.004 arcsec [2]. However, the microvibrations due to the onboard equipment in spacecraft will seriously degrade the image quality of the space telescope [3]. The microvibration sources include control moment gyros, reaction wheel assemblies, cryocoolers, solar panel deployment actuators, and other motion devices [4]. During the past decades, many methods have been developed to diminish the vibrations from instruments. Vibration isolation is one of the vibration suppression techniques widely applied to solve this problem [5–24].

Vibration isolation can be categorized into passive isolation, active isolation, and active–passive isolation. Passive isolation is widely used to attenuate vibrations induced by spacecraft because of its characteristics of reliability, simply maintenance, low cost, etc. [5–8]. The HST is probably the best-known example of a space telescope that applies a passive isolator to achieve its science mission [6], as well as the X-Ray Astrophysics Facility [7] and the James Webb Space Telescope [8]. Since the microvibrations are usually multiaxial, vibration isolation for the space telescope should have multiple-degrees-of-freedom characteristics. So far, many multiaxis isolators have been investigated, and the Gough–Stewart isolation system (GSIS) is the most widely used because of the advantages of control proposes [9–13], such as the ultraquiet platform [14], the Miniature Vibration Isolation System [15], and the six-axis vibration isolation [16]. Until now, many researchers have focused on how to design the parameters of the vibration isolator element of the vibration isolation system (VIS) to provide optimal damping. Some vibration isolators have been designed, such as the D-strut sets developed by Honeywell, Inc. [17–21]. The effectiveness of these D-struts was sufficiently proved by the Hubble reaction wheel isolation system [6] and the vibration isolation and suppression system [22]. However, research on the configuration optimization of the GSIS is still rare. Most of the research focused on the cubic hexapod. For example, Thayer et al. [23] designed and tested a unique hexapod system for spaceborne interferometry missions. Zhang et al. [11,12] and Zhang and Xu [13] conducted substantial studies on the isolation effect of the GSIS. Lee et al. [24] also developed a passive vibration isolation platform for low-amplitude vibration using a cubic hexapod. The multiaxis isolation effect of the platform was tested with a prototype reaction wheel model. Nevertheless, the VIS with the cubic hexapod configuration cannot achieve the complete dynamic decoupling in the case where the payload's centroid does not coincide with the center of the upper joint points [25].

In general, the amplitude-frequency curve of the relationship between the input and output of the system is used to assess the isolation effect of a VIS. The basic objective of a VIS applied to the optical payload is to improve the image quality of the optical system. As a result, not only the amplitude-frequency curve but also the integrated optomechanical analysis is required to evaluate the isolation effect of the VIS. Miller et al. [26] proposed a comprehensive framework for integrated modeling known as the disturbances optics controls structures, which was used in the Terrestrial Planet Finder mission [27] and the Space Interferometry Mission [28]. Some analogous research has been done, such as the integrated technology model [29] and the structural–thermal–optical [30]. However, the aforementioned integrated optomechanical analysis methods are complicated and require an amount of data exchange among different software. It may be more efficient to adopt a concise integrated optomechanical analysis to verify the isolation effect of the VIS.

In this Note, a way to obtain the optimal design parameters and configuration of the VIS designed for the space optical device is discussed. The general dynamic model of the VIS, including the optical payload, is carried out by means of the Newton–Euler method. The algebraic expressions, which could be used to calculate the natural frequencies of VIS applied for the payload for which the centroid does not coincide with the center of the upper joint points, are derived. In addition, two kinds of optimal design methods using local dynamic isotropy and dynamic isotropy are proposed to reduce the coupling effect and obtain the optimal design parameters. By using the aforementioned methods, a VIS can be developed. To verify the isolation effect of the VIS, an integrated optomechanical analysis based on a finite element method is adopted. This integrated optomechanical analysis approach can overcome the drawback of abundant data exchange among different software.

II. Optical and Structural Modeling

The optical layout of the telescope studied in this Note is depicted in Fig. 1. It is a classic Cassegrain system with a parabolic primary mirror and a hyperbolic secondary mirror. The material of the primary mirror and the secondary mirror is Zerodur™, to minimize the impact of thermal distortion [31]. The telescope consists of two main parts: the primary mirror assembly and the second mirror assembly. The primary mirror assembly, which includes the primary mirror, the

Received 19 December 2014; revision received 4 February 2015; accepted for publication 5 February 2015; published online 8 April 2015.

*Ph.D. Candidate, Space Robotics Engineering Center, No. 3888 Dong Nanhu Road; currently University of Chinese Academy of Sciences, No. 19A Yuquan Road, Beijing 100049, PRC; yangjeff2013@163.com.

†Associate Researcher, Space Robotics Engineering Center, No. 3888 Dong Nanhu Road; xuzhenbang@gmail.com.

‡Researcher, Space Robotics Engineering Center, No. 3888 Dong Nanhu Road; wuqw@ciomp.ac.cn.

§Associate Researcher, Space Robotics Engineering Center, No. 3888 Dong Nanhu Road; sabina_wzs@aliyun.com.

¶Research Assistant, Space Robotics Engineering Center, No. 3888 Dong Nanhu Road; cicelihang@126.com.

**Research Assistant, Space Robotics Engineering Center, No. 3888 Dong Nanhu Road; xiaoxiao4032@126.com.

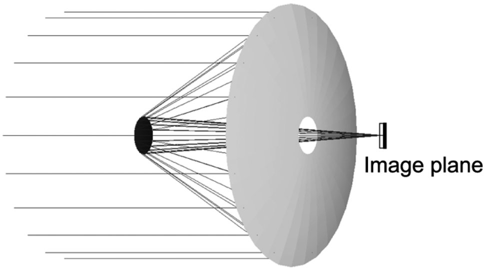

Fig. 1 Optical layout of the telescope.

main flexure, and the main plate, is attached to the support ring. The second mirror assembly, which contains the second mirror, the minor flexure, and the minor ring, is fixed to the support frame. The detailed structure of the telescope is shown in Fig. 2.

III. Dynamic Model

The properly designed VIS is placed between the optical payload and the spacecraft, as shown in Fig. 3a. The whole isolation system consists of a payload platform, six isolation struts, and a base platform. Flexure joints are used to connect isolator struts and the payload platform instead of ball joints. The isolation strut is a viscous passive isolator, which can be simplified as a damping-spring model in which the spring is parallel to the damper, as shown in Fig. 3b.

The coordinate frames of the VIS are shown in Fig. 4a, in which $\{B\}$ is the base frame and $\{P\}$ is the body frame. The base frame $\{B\}$ with origin O_B and the body frame $\{P\}$ with origin O_P are embedded in the base platform and the payload platform, respectively. Vector $\boldsymbol{q} = [\boldsymbol{t}, \boldsymbol{q}_P]^T$ denotes the pose of the body frame $\{P\}$ relative to the base frame $\{B\}$, in which the vector $\boldsymbol{t}$ describes the position of the origin O_P with respect to frame $\{B\}$ and the vector $\boldsymbol{q}_P = [\gamma, \beta, \alpha]^T$ describes the posture of frame $\{P\}$ with respect to frame $\{B\}$. The upper joint points and the lower joint points are denoted with ${}^P p_i$ in frame $\{P\}$ and ${}^B p_i$ in frame $\{B\}$, respectively. The radii of the payload and base platforms are represented by R_P and R_B, respectively. The angle between P_6 and P_1 is denoted by φ. The angle between B_6 and B_1 is denoted by θ, which is illustrated in Fig. 4b.

The dynamic equations of the optical payload with the VIS can be derived by using the Newton–Euler method as

$$M\ddot{\boldsymbol{q}} + V(\boldsymbol{q}, \dot{\boldsymbol{q}})\dot{\boldsymbol{q}} + K\boldsymbol{q} = \boldsymbol{F} \tag{1}$$

where M is the mass matrix of the optical payload in frame $\{B\}$; $V(\boldsymbol{q}, \dot{\boldsymbol{q}})$ is the Coriolis and centrifugal coefficients matrix; K is the stiffness matrix (see the Appendix); $\boldsymbol{F}$ is the vector of the generalized applied forces; and $\boldsymbol{q}$, $\dot{\boldsymbol{q}}$, and $\ddot{\boldsymbol{q}}$ are the displacement, velocity, and acceleration vectors of the payload platform with respect to frame

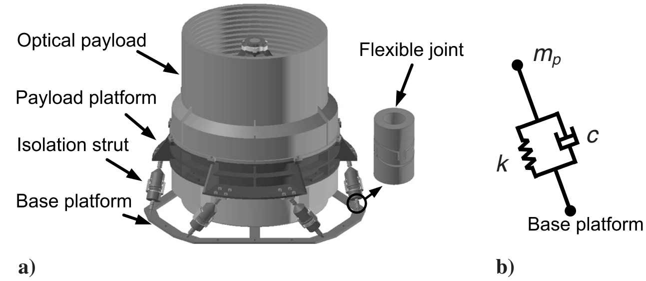

Fig. 3 Vibration isolation system: a) geometric model of the isolation system, and b) isolation strut.

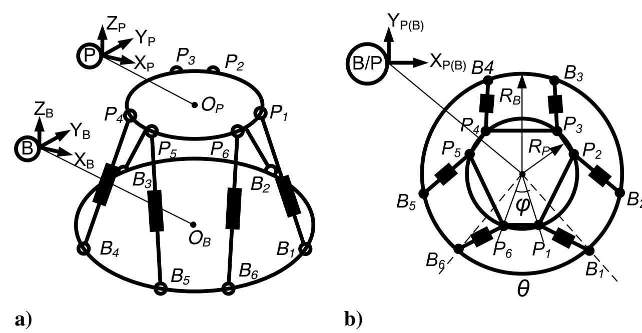

Fig. 4 Configuration of vibration isolation system: a) isometric view, and b) vertical view.

$\{B\}$, respectively: they all contain translation and angular components.

In the dynamic problems of the VIS, the natural characteristics of the VIS are important. The Coriolis and centrifugal force terms as the square terms of velocity may be neglected when the velocity is small. The mass of the isolation struts is small compared with that of the optical payload, so it can also be ignored. The free vibration of the optical payload with the VIS may be described as

$$M\ddot{\boldsymbol{q}} + C\dot{\boldsymbol{q}} + K\boldsymbol{q} = 0 \tag{2}$$

where C is the damping matrix; see the Appendix. The natural frequencies and mode shapes (or eigenvectors) of the VIS can be obtained by solving this equation with numerical methods.

IV. Optimization of the VIS

At the design stage of the isolation system, getting the algebraic expressions used for calculating the natural frequencies of the VIS is very useful for us to perform an optimal design, whereas obtaining

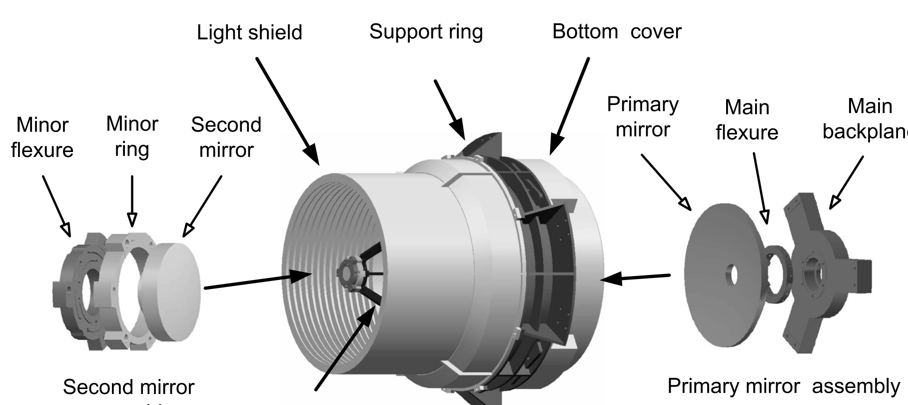

Fig. 2 Structure of the telescope.

the algebraic expressions, which are suitable to any payload, is very difficult. Fortunately, the algebraic expressions may be obtained when the payload inertia matrix is diagonal and, at the same time, the pose of the body frame has zero orientation and center position with $\boldsymbol{q} = [0, 0, H, 0, 0, 0]^T$. The telescope studied in this Note satisfies the aforementioned requirements, so the algebraic expressions can be used to optimize the isolation system.

As we know, the configuration of the VIS can greatly affect the isolation effect. The aim of our design is to find an optimal configuration with which the natural frequencies of the VIS are mostly close to each other and the resonance frequency bandwidth can be reduced. According to the literature [25], it is known that the eigenvalues of the mass matrix M are closest to each other and the degrees of freedom (DOFs) of X and RY, as well as Y and RX, are fully decoupled when the payload's center of mass h coincides with the compliance center h^* expressed by Eq. (3). Based on the preceding research, it could be concluded that 1) the natural frequencies of the VIS are closest to each other, and 2) the movements of the six DOFs are decoupled on the condition that expression (3) is satisfied.

Hence, at the early design stage of the VIS, the following requirement should be satisfied:

$$h = h^* = \frac{-R_P[R_P - R_B\ \cos(\theta - \varphi/2)]}{R_P^2 + R_B^2 - 2R_P R_B\ \cos(\theta - \varphi/2)} \tag{3}$$

where $\varphi \neq \theta$, and H is the height of the body frame with respect to the base frame $\{B\}$.

A. Optimal Design Based on Local Dynamic Isotropy

The goal of the optimal design based on local dynamic isotropy is to get the design parameters of the Gough–Stewart-platform-based VIS with a minimum ratio of the maximum natural frequency to the minimum natural frequency. Thus, an optimal design problem in one pose can be expressed as

$$\kappa = \frac{\omega_{\max}}{\omega_{\min}} = \frac{\sqrt{k\lambda_{\max}(M_{\text{act}}^{-1})}}{\sqrt{k\lambda_{\min}(M_{\text{act}}^{-1})}} \tag{4}$$

where $M_{\text{act}} = J^{-T}MJ^{-1}$ is the joint space generalized mass matrix. The maximum eigenvalues and the minimum eigenvalues of M_{act}^{-1} are $\lambda_{\max}(M_{\text{act}}^{-1})$ and $\lambda_{\min}(M_{\text{act}}^{-1})$, respectively [32].

In this Note, some results from previous works [25,32,33] are applied to deal with the natural frequency problems of the VIS. Through further study, the first six natural frequencies of the VIS can be expressed through the following algebraic expressions:

$$f_1 = \frac{1}{2\pi}\sqrt{\frac{6k}{m}\cdot\frac{H^2}{R_P^2 + R_B^2 - 2R_P R_B\ \cos(\theta - \varphi/2)} + H^2} \tag{5}$$

$$f_2 = \frac{1}{2\pi}\sqrt{\frac{6k}{I_{zz}}\cdot\frac{R_P^2 R_B^2\ \sin(\theta - \varphi/2)^2}{R_P^2 + R_B^2 - 2R_P R_B\ \cos(\theta - \varphi/2)} + H^2} \tag{6}$$

$$f_{3,4} = \frac{1}{2\pi}\sqrt{\frac{3k[\Lambda_{yy} \pm ({\Lambda_{yy}}^2 - 4(m/I_{yy})H^2 R_P^2 R_B^2 \sin(\theta - \varphi/2)^2)^{1/2}]}{2m[R_P^2 + R_B^2 - 2R_P R_B \cos(\theta - \varphi/2) + H^2]}} \tag{7}$$

$$f_{5,6} = \frac{1}{2\pi}\sqrt{\frac{3k[\Lambda_{xx} \pm ({\Lambda_{xx}}^2 - 4(m/I_{xx})H^2 R_P^2 R_B^2 \sin(\theta - \varphi/2)^2)^{1/2}]}{2m[R_P^2 + R_B^2 - 2R_P R_B \cos(\theta - \varphi/2) + H^2]}} \tag{8}$$

To guarantee that no singularity is possible for the VIS, $H \neq 0$ and $\theta \neq \varphi$ should be met.

B. Optimal Design Based on Dynamic Isotropy

According to the initial analysis, when the payload's center of mass coincides with the compliance center h^* and the first six natural frequencies are equal to each other, the VIS can achieve a better vibration isolation effect. If we let $f_1 = f_2 = f_3 = f_4 = f_5 = f_6$, the requirements specified by Eq. (9) should be met for the payload:

$$I_{zz} = 4I_{yy} = \frac{3mR_P^2 R_B^2}{2(R_P^2 - R_B R_P + R_B^2)} \tag{9}$$

In practice, it is difficult to satisfy Eq. (9), which may require laborious work and tedious procedures, as reported in literature [34].

In some applications, it is expected that the frequency bandwidths are uniform just in translation, or angular motion, or by combining both of them. For the vibration attenuation of telescope, the VIS is mainly used to isolate the microvibrations of the spacecraft in angular motion, which largely degrade the image quality of the telescope compared with that caused by translational vibration. Therefore, the natural frequencies of rotational direction should be equal to each other. When $f_2 = f_3 = f_5$, the following equations may be obtained:

$$H^* = \sqrt{2}\sqrt{\frac{I_{yy}}{I_{zz}}\left(R_P^2 + R_B^2 - 2R_P R_B\ \cos\left(\frac{\theta - \varphi}{2}\right)\right)} \tag{10}$$

$$f_1^* = \frac{1}{2\pi}\sqrt{\frac{12kI_{yy}}{m(I_{zz} + 2I_{yy})}} \tag{11}$$

$$f_2^* = f_3^* = f_5^* = \frac{1}{2\pi}\sqrt{\frac{6kR_P^2 R_B^2 \sin^2(\theta - \varphi/2)}{R_P^2 + R_B^2 - 2R_P R_B\ \cos(\theta - \varphi/2)}\cdot\frac{1}{I_{zz} + 2I_{yy}}} \tag{12}$$

$$f_4^* = f_6^* = \frac{1}{2\pi}\sqrt{\frac{3kI_{zz}}{m(I_{zz} + 2I_{yy})}} \tag{13}$$

C. Parameter Optimization Design of the VIS

For the space telescope, the natural frequencies of the VIS should meet a certain range. The high-frequency isolation effect increases with the decrease of the natural frequency of the VIS, whereas the attitude control stabilization of the spacecraft might be reduced. Therefore, there is a tradeoff between the isolation effect and the attitude control stabilization to choose the natural frequency range of the VIS. The spacecraft attitude control bandwidth is about 0.1 Hz, so the isolation system should be roughly an order of magnitude stiffer than that. A target of $1 \sim 3$ Hz is set for the range of natural frequencies of the isolation system [8].

The objective function of the two optimization methods is expressed as

$$\min\left\{\kappa = \frac{\omega_{\max}}{\omega_{\min}} = \frac{\sqrt{\lambda_{\max}(M_{\text{act}}^{-1})}}{\sqrt{\lambda_{\min}(M_{\text{act}}^{-1})}}\right\} \tag{14}$$

The constraint conditions of the local dynamic isotropy-based optimization method are described as

Table 1 Parameters of the isolation system based on two different optimization methods

Notation	Specification	Local dynamic isotropy	Dynamic isotropy
R_P	Payload platform radius	0.178 m	0.178 m
R_B	Base platform radius	0.200 m	0.200 m
φ	Payload platform central angle	0 deg	40 deg
θ	Base platform central angle	120 deg	140 deg
k	Stiffness of isolation strut	546.4 N · m^{-1}	596.9 N · m^{-1}
H	Height of payload platform	0.0951 m	0.0956 m

Table 2 Parameters of the isolation system based on two different optimization methods

Mode	Local dynamic isotropy, Hz	Dynamic isotropy, Hz
First	1.00	1.05
Second	1.00	1.05
Third	1.92	2.04
Fourth	1.92	2.18
Fifth	1.93	2.18
Sixth	1.95	2.18

$$\begin{cases} 0 \le \varphi \le \frac{\pi}{3} \\ \theta + \varphi = \frac{2\pi}{3} \\ \theta \ne \varphi \\ 500 \le k \le 5000 \text{ N} \cdot \text{m}^{-1} \\ 0.2 \le R_B \le 0.5 \text{ m} \\ 0.095 \le H \le 0.6 \text{ m} \\ H \ne 0 \end{cases}$$

The constraint conditions of the dynamic isotropy-based optimization method are described as

$$\begin{cases} 0 \le \varphi \le \frac{\pi}{3} \\ \theta \ne \varphi \\ 500 \le k \le 5000 \text{ N} \cdot \text{m}^{-1} \\ H \ne 0 \end{cases}$$

The design parameters of the VIS optimized with the MATLAB *fmincon* optimization function are listed in Table 1. By using expressions (5–8,11–13), the first six natural frequencies may be obtained, as shown in Table 2.

According to Table 2, there is no substantial difference between the results of the two optimization methods. The natural frequency ranges of the two methods are almost the same. The three rotational frequencies obtained by using the dynamic isotropy are the same, which is more helpful in improving the image quality of the telescope. Therefore, the design parameters of the VIS based on the dynamic isotropy are adopted.

Substituting the design parameters and natural frequencies of the VIS into Eq. (2), the mode shapes are obtained, which represent the position and orientation of the payload corresponding to each natural frequency. The modal matrix obtained from Eq. (2) is rearranged according to the natural frequency sequence as described with expression (15). As shown in expression (15), the diagonal elements are much larger than other elements. It indicates that the VIS is almost completely decoupled on all six axes of vibration:

$$\boldsymbol{U} = \begin{bmatrix} 1 & 0.02 & 0 & 0 & 0 & 0 \\ 0.02 & -1 & 0 & 0 & 0 & 0 \\ 0 & 0 & 1 & 0 & 0 & 0 \\ 0 & 0 & 0 & -1 & 0 & 0 \\ 0 & 0 & 0 & 0 & 1 & -0.03 \\ 0 & 0.02 & 0 & 0 & -0.03 & 1 \end{bmatrix} \tag{15}$$

V. Integrated Optomechanical Analysis

Line-of-sight (LOS) jitter is the time-varying motion of the image on the detector plane, which is due to the internal or external dynamic loads acting on an optical system [35]. For flexible optics, such as the primary mirror of the reflective optical system, the microvibrations may change the shape of the optical surfaces. So, the optic cannot be regarded as a rigid body. It is realistic to account for the deformations of the optical surfaces and then compute the average rigid-body motions. For optical surfaces, which are represented by a grid of nodes, the rigid-body motion of the surface may be computed as the area-weight average motion. Let T_x, T_y, and T_z, describe the translations along coordinate axes and R_x, R_y, and R_z, describe the rotations about coordinate axes. The sign of the rotation angle is determined by the right-hand rule.

The fit displacement of node i due to these motions is

$$\begin{aligned} d\tilde{x}_i &= T_x + z_i R_y - y_i R_z \quad d\tilde{y}_i = T_y - z_i R_x + x_i R_z \\ d\tilde{z}_i &= T_z + y_i R_x - x_i R_y \end{aligned} \tag{16}$$

where $d\tilde{x}_i$, $d\tilde{y}_i$, and $d\tilde{z}_i$, are, respectively, the displacements at node positions x_i, y_i, and z_i, due to rigid-body motions. The error E, is defined as the difference between the actual optical surface nodal displacements dx_i, dy_i, and dz_i and the rigid-body nodal displacements $d\tilde{x}_i$, $d\tilde{y}_i$, and $d\tilde{z}_i$. A least-squares fit may be used to compute the average rigid-body motions of a given surface:

$$E = \sum_{i=1}^{n} w_i(dx_i - d\tilde{x}_i)^2 + w_i(dy_i - d\tilde{y}_i)^2 + w_i(dz_i - d\tilde{z}_i)^2 \tag{17}$$

where w_i is the weighting function of node i.

To find the average rigid-body motions $(T_x, T_y, T_z, R_x, R_y, R_z)$, we minimize E by taking partial derivatives with respect to each term and setting the result to zero. These equations can be written as

$$\begin{cases} \frac{\partial E}{\partial T_x} = \sum_{i=1}^{n} w_i[dx_i - (T_x + z_i R_y - y_i R_z)] = 0 \\ \frac{\partial E}{\partial T_y} = \sum_{i=1}^{n} w_i[dy_i - (T_y - z_i R_x + x_i R_z)] = 0 \\ \frac{\partial E}{\partial T_z} = \sum_{i=1}^{n} w_i[dz_i - (T_z + y_i R_x - x_i R_y)] = 0 \\ \frac{\partial E}{\partial R_x} = \sum_{i=1}^{n} w_i\{[dy_i - (T_y - z_i R_x + x_i R_z)]z_i - [dz_i - (T_z + y_i R_x - x_i R_y)]y_i\} = 0 \\ \frac{\partial E}{\partial R_y} = \sum_{i=1}^{n} w_i\{-[dx_i - (T_x + z_i R_y - y_i R_z)]z_i + [dz_i - (T_x + y_i R_x - x_i R_y)]x_i\} = 0 \\ \frac{\partial E}{\partial Z_z} = \sum_{i=1}^{n} w_i\{[dx_i - (T_x + z_i R_y - y_i R_z)]y_i - [dy_i - (T_y - z_i R_x + x_i R_z)]x_i\} = 0 \end{cases} \tag{18}$$

Table 3 Six load cases acting on the telescope

Load case	Acceleration	Frequency range, Hz
Translational vibration along the x axis	1 mg	$0.1 \sim 103$
Translational vibration along the y axis	1 mg	$0.1 \sim 103$
Rotational vibration around the x axis	10^{-6} arcseconds^2	$0.1 \sim 103$
Rotational vibration around the y axis	10^{-6} arcseconds^2	$0.1 \sim 103$
Translational vibration along the z axis	1 mg	$0.1 \sim 103$
Rotational vibration around the z axis	10^{-6} arcseconds^2	$0.1 \sim 103$

Table 4 Specifications of the cubic hexapod based isolator

Notation	Specification	Value
R_P	Payload platform radius	0.178 m
R_B	Base platform radius	0.178 m
φ	Payload platform central angle	0 deg
θ	Base platform central angle	120 deg
K	Stiffness of isolation strut	$710\ \mathrm{N \cdot m^{-1}}$
H	Height of payload platform	0.1259 m

Table 5 Natural frequencies and mode shapes of the cubic hexapod based isolator

Mode	Natural frequencies, Hz	Mode shapes
First	1.00	$[0.00,\ -0.13,\ 0.00,\ 1.00,\ 0.01\ \ 0.00]^T$
Second	1.00	$[0.13,\ 0.00,\ 0.00,\ -0.01,\ 1.00\ \ 0.00]^T$
Third	1.59	$[0.00,\ 0.00,\ 1.00,\ 0.00,\ 0.00,\ 0.00]^T$
Fourth	2.34	$[0.00,\ 0.12,\ 0.00,\ 1.00,\ 0.00\ \ 0.00]^T$
Fifth	2.34	$[0.12,\ 0.00,\ 0.00,\ 0.00,\ -1.00\ \ 0.00]^T$
Sixth	2.90	$[0.00,\ 0.00,\ 0.00,\ 0.00,\ 0.00,\ 1.00]^T$

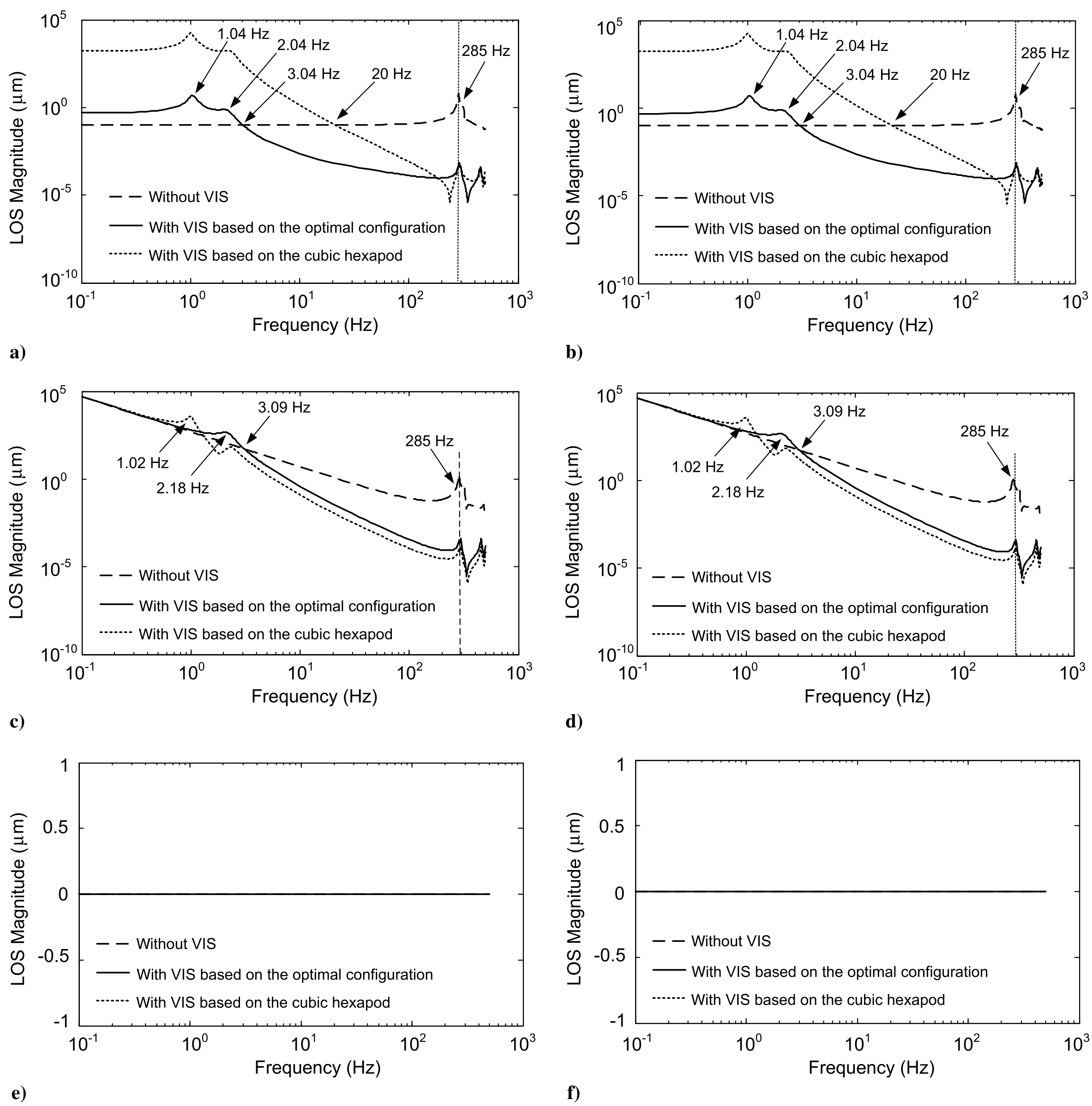

Fig. 5 Comparison of the LOS with and without the VIS at different cases.

Substituting the nodal data of optical surfaces into Eq. (18) and solving these equations, the average rigid-body motions $(T_x, T_y, T_z, R_x, R_y, R_z)$ are obtained. The average rigid-body motions can also be calculated by interpolation elements in MSC.NASTRAN software [35].

Image motion, as a function of time and frequency, can be computed using finite element analysis. This method assumes that the image motion is a linear function of the optical element displacement [35,36]. The relationship of the image motion $(\Delta x, \Delta y)$ and the average rigid-body motions $([T]_{\text{optics}})$ can be expressed as

$$\begin{Bmatrix} \Delta x \\ \Delta y \end{Bmatrix} = [L]_{\text{img}}[T]_{\text{optics}} \tag{19}$$

where $[L]_{\text{img}}$ is the optical sensitivity coefficients, which can be obtained from an optical design code. The image motion equation can be entered directly into most finite element programs.

VI. Analysis Results

To verify the effectiveness of the VIS on improving the image quality of the optical system, the LOS jitters of the optical system without VIS, with the VIS based on the optimal configuration, and with the VIS based on the cubic hexapod are calculated. Six different load cases are considered, as shown in Table 3. The disturbance accelerations are applied on the base platform in six directions. The specifications of the VIS based on the cubic hexapod are provided in Table 4. Its natural frequencies and mode shapes are shown in Table 5. The following analysis is carried out using MSC/NASTRAN.

Figure 5 depicts the comparison of the LOS magnitude of image against frequency for different load cases: a) translational vibration along the x axis, b) translational vibration along the y axis, c) rotational vibration around the x axis, d) rotational vibration around the y axis, e) translational vibration along the z axis, and f) rotational vibration around the z axis. The dashed lines denote the LOS magnitude of the image without VIS, the solid curves denote that with the VIS based on the optimal configuration, and the dotted line denotes that with the VIS based on the cubic hexapod. From Fig. 5, it can be concluded that the VIS could efficiently reduce the LOS jitter of the optical system due to the microvibrations. Figure 5 shows that the VIS improves the image quality at high frequency but degrades the image quality at low frequency. A fast steering mirror, which is usually adopted to reduce the jitter due to spacecraft at low frequency, may be used to overcome this drawback [37]. Because the structure of the optical payload is symmetric, the curves in Figs. 5a and 5b are almost identical, as well as in Figs. 5c and 5d and in Figs. 5e and 5f.

According to Figs. 5a and 5b, it can be found that the VIS based on the optimal configuration can achieve a better isolation effect for the translational vibration in contrast to the VIS based on the cubic configuration, which benefits from the decoupling as stated in expression (15).

From Figs. 5c and 5d, it may be noted that the two kinds of VIS can achieve almost the same isolation effect for rotational vibrations. However, for the VIS based on the cubic hexapod, there are two resonance peaks at low frequency, whereas for the VIS based on the optimal configuration, there is one resonance peak. A peak occurs at a frequency of 285 Hz, which is attributed to the elastic resonance of the support frame.

The LOS magnitudes of the images shown in Figs. 5e and 5f are a zero constant. It means that microvibrations along the z axis and around the z axis have no influence on the image quality of the optical system because the two kinds of motions do not affect the optic axis direction.

VII. Conclusions

This Note addresses the design and analysis of a Gough–Stewart–platform-based vibration isolation system used for the space telescope. Two kinds of different optimization methods are proposed to optimize the vibration attenuation performance of the VIS. An integrated optomechanical analysis is applied to verify the effectiveness of the VIS. The simulation and results show that the VIS can efficiently improve the image quality of the telescope at a frequency above 3 Hz. It can be concluded that this VIS is suitable for the vibration attenuation of the telescope, and the methods including the design of the isolation system and the integrated optomechanical analysis are applicable to the vibration attenuation of other space telescopes.

Appendix: Detailed Expressions for Some Intermediate Terms

The following are the terms in Eq. (1):

$$M = \begin{bmatrix} mE_3 & m \cdot {}^B_PR \cdot {}^P\tilde{p}_c^T \cdot {}^B_PR^T \\ m \cdot {}^B_PR \cdot {}^P\tilde{P}_c \cdot {}^B_PR^T & {}^B_PR \cdot {}^PI \cdot {}^B_PR^T \end{bmatrix}$$

where the center of mass ${}^Pp_c$ is a 3×1 vector, the pre-superscript P denotes the body frame axes, m is the payload mass, E_3 is 3×3 identity matrix, ${}^PI$ is the inertia matrix with respect to frame $\{P\}$, ${}^P\tilde{p}_c$ denotes a skew symmetry matrix of a spatial vector ${}^Pp_c$, ${}^P\tilde{p}_c^T$ is the transpose of ${}^P\tilde{p}_c$, ${}^B_PR$ is the rotation matrix relating the VIS's coordinate system, and ${}^B_PR^T$ is the transpose of ${}^B_PR$:

$${}^B_PR = \begin{bmatrix} \cos\alpha \cdot \cos\beta & \cos\alpha \cdot \sin\beta \cdot \sin\gamma - \sin\alpha \cdot \cos\gamma & \cos\alpha \cdot \sin\beta \cdot \cos\gamma + \sin\alpha \cdot \sin\gamma \\ \sin\alpha \cdot \cos\beta & \sin\alpha \cdot \sin\beta \cdot \sin\gamma + \cos\alpha \cdot \cos\gamma & \cos\alpha \cdot \sin\beta \cdot \cos\gamma - \cos\alpha \cdot \sin\gamma \\ -\sin\beta & \cos\beta \cdot \sin\gamma & \cos\beta \cdot \cos\gamma \end{bmatrix} \quad K = k \cdot J^TJ \quad C = c \cdot J^TJ$$

where k and c are the stiffness coefficient and damping coefficient of the strut, respectively. J^T is the transpose of the Jacobian J, and J is defined as

$$J = \begin{bmatrix} {}^B\boldsymbol{l}_{n1}^T, ({}^P_BR \cdot {}^Pp_1 \times {}^B\boldsymbol{l}_{n1})^T \\ {}^B\boldsymbol{l}_{n2}^T, ({}^P_BR \cdot {}^Pp_2 \times {}^B\boldsymbol{l}_{n2})^T \\ {}^B\boldsymbol{l}_{n3}^T, ({}^P_BR \cdot {}^Pp_3 \times {}^B\boldsymbol{l}_{n3})^T \\ {}^B\boldsymbol{l}_{n4}^T, ({}^P_BR \cdot {}^Pp_4 \times {}^B\boldsymbol{l}_{n4})^T \\ {}^B\boldsymbol{l}_{n5}^T, ({}^P_BR \cdot {}^Pp_5 \times {}^B\boldsymbol{l}_{n5})^T \\ {}^B\boldsymbol{l}_{n6}^T, ({}^P_BR \cdot {}^Pp_6 \times {}^B\boldsymbol{l}_{n6})^T \end{bmatrix}$$

where ${}^B\boldsymbol{l}_{n1}(i = 1 \sim 6)$ is the unit vector of the strut in the base frame.

The following are the terms in expressions (7) and (8):

$$\begin{aligned} \Lambda_{yy} = \frac{m}{I_{yy}} \Bigg[& \left(R_P^2 + R_B^2 - 2R_PR_B \cos\left(\frac{\theta - \varphi}{2}\right) \right) h^2 \\ & + 2R_PH\left(R_P - R_B \cos\left(\frac{\theta - \varphi}{2}\right) \right) h + R_P^2H^2 \Bigg] \\ & + \left[R_P^2 + R_B^2 - 2R_PR_B \cos\left(\frac{\theta - \varphi}{2}\right) \right] \\ \Lambda_{xx} = \frac{m}{I_{xx}} \Bigg[& \left(R_P^2 + R_B^2 - 2R_PR_B \cos\left(\frac{\theta - \varphi}{2}\right) \right) h^2 \\ & + 2R_PH\left(R_P - R_B \cos\left(\frac{\theta - \varphi}{2}\right) \right) h + R_P^2H^2 \Bigg] \\ & + \left[R_P^2 + R_B^2 - 2R_PR_B \cos\left(\frac{\theta - \varphi}{2}\right) \right] \end{aligned}$$

where I_{xx} and I_{yy} are the moments of inertia.

Acknowledgments

This work is supported by the National Natural Science Foundation of China under grant no. 11302222 and the Innovation Foundation of the Changchun Institute of Optics, Fine Mechanics and Physics, Chinese Academy of Sciences under grant no. Y4CX1SS141.

Reference

[1] Crocker, J. H., "Fixing the Hubble Space Telescope," *Proceedings of the SPIE: Space Astronomical Telescopes and Instruments*, Vol. 1494, SPIE, Bellingham, WA, 1991, pp. 2–8.
doi:10.1117/12.46709

[2] Bronowicki, A. J., and Innis, J. W., "A Family of Full Spacecraft-to-Payload Isolators," *Technology Review Journal*, Vol. 13, Fall/Winter 2005, pp. 21–41.

[3] Toyoshima, M., Takayama, Y., and Kunimori, H., "In-Orbit Measurements of Spacecraft Microvibrations for Satellite Laser Communication Links," *Optical Engineering*, Vol. 49, No. 8, 2010, Paper 083604.
doi:10.1117/1.3482165

[4] Hu, Q., Jia, Y. H., and Xu, S. J., "Adaptive Suppression of Linear Structural Vibration Using Control Moment Gyroscopes," *Journal of Guidance, Control, and Dynamics*, Vol. 37, No. 3, May–June 2014, pp. 990–996.
doi:10.2514/1.62267

[5] Kamesh, D., Pandiyan, R., and Ghosal, A., "Passive Vibration Isolation of Reaction Wheel Disturbances Using a Low Frequency Flexible Space Platform," *Journal of Sound and Vibration*, Vol. 331, No. 6, 2012, pp. 1310–1330.
doi:10.1016/j.jsv.2011.10.033

[6] Davis, L. P., and Wilson, J. F., "Hubble Space Telescope Reaction Wheel Assembly Vibration Isolation System," NASA Rept. N87-22702, 1986, pp. 669–690.

[7] Pendergas, K. J., and Schauwecker, C. J., "Use of a Passive Reaction Wheel Jitter Isolation System to Meet the Advanced X-Ray Astrophysics Facility Imaging Performance Requirements," *Proceedings of the SPIE: Space Telescopes and Instruments V*, Vol. 3356, SPIE, Bellingham, WA, 1998, pp. 1078–1094.
doi:10.1117/12.324508

[8] Bronowicki, A. J., "Vibration Isolator for Large Space Telescopes," *Journal of Spacecraft and Rockets*, Vol. 43, No. 1, 2006, pp. 45–53.
doi:10.2514/1.12036

[9] de Marneffe, B., Avraam, M., Deraemaeker, A., Horodinca, M., and Preumont, A., "Vibration Isolation of Precision Payloads: A Six-Axis Electromagnetic Relaxation Isolator," *Journal of Guidance, Control, and Dynamics*, Vol. 32, No. 2, 2009, pp. 395–401.
doi:10.2514/1.39414

[10] Spanos, J., Rahman, Z., and Blackwood, G., "A Soft 6-Axis Active Vibration Isolator," *Proceedings of the IEEE American Control Conference*, Vol. 1, IEEE, Piscataway, NJ, 1995, pp. 412–416.
doi:10.1109/ACC.1995.529280

[11] Zhang, Y., Zhang, J. R., and Xu, S. J., "Influence of Flexible Solar Arrays on Vibration Isolation Platform of Control Moment Gyroscopes," *Acta Mechanica Sinica*, Vol. 28, No. 5, 2012, pp. 1479–1487.
doi:10.1007/s10409-012-0148-x

[12] Zhang, Y., Zhang, J. R., and Xu, S. J., "Parameters Design of Vibration Isolation Platform for Control Moment Gyroscopes," *Acta Mechanica Sinica*, Vol. 81, No. 2, 2012, pp. 645–659.

[13] Zhang, Y., and Xu, S. J., "Vibration Isolation Platform for Control Moment Gyroscopes on Satellites," *Journal of Aerospace Engineering*, Vol. 25, No. 4, 2012, pp. 641–652.
doi:10.1061/(ASCE)AS.1943-5525.0000156

[14] Chen, H. J., Bishop, R., and Agrawal, B., "Payload Pointing and Active Vibration Isolation Using Hexapod Platform," *44th AIAA/ASME/ASCE/AHS/ASC Structures, Structural Dynamics, and Materials Conference*, AIAA Paper 2003-1643, April 2003, pp. 1–19.
doi:10.2514/6.2003-1643

[15] McMickell, M. B., Kreider, T., Hansen, E., Davis, T., and Gonzalez, M., "Optical Payload Isolation Using the Miniature Vibration Isolation System (MVIS-II)," *Proceedings of the SPIE: Industrial and Commercial Applications of Smart Structures Technologies 2007*, Vol. 6257, SPIE, Bellingham, WA, 2007, Paper 652703.
doi:10.1117/12.715446

[16] Rahman, Z. H., Spanos, J. T., and Laskin, R. A., "Multiaxis Vibration Isolation, Suppression, and Steering System for Space Observational Applications," *Proceedings of the SPIE: Telescope Control Systems III*, Vol. 3351, SPIE, Bellingham, WA, 1998, pp. 73–81.
doi:10.1117/12.308821

[17] Anderson, E., Trubert, M., Fanson, J., and Davis, P., "Testing and Application of a Viscous Passive Damper for Use in Precision Truss Structures," *32nd Structures, Structural Dynamics, and Materials Conference*, AIAA Paper 1991-0996, 1991, pp. 2796–2808.

[18] Davis, P., Cunningham, D., and Harrell, J., "Advanced 1.5 Hz Passive Viscous Isolation System," *35th Structures, Structural Dynamics, and Materials Conference*, AIAA Paper 1994-1651, 1994, pp. 2655–2665.
doi:10.2514/6.1994-1651

[19] Davis, P., Cunningham, D., Bicos, A., and Enright, M., "Adaptable Passive Viscous Damper (An Adaptable D-Strut ZerodurTM)," *Proceedings of the SPIE: Smart Structures and Materials 1994: Passive Damping*, Vol. 2193, SPIE, Bellingham, WA, 1994, pp. 47–58.
doi:10.1117/12.174114

[20] Davis, L. P., Carter, D. R., and Hyde, T. T., "Second Generation Hybrid D-strut," *Proceedings of the SPIE: Smart Structures and Materials 1995: Passive Damping*, Vol. 2445, SPIE, Bellingham, WA, 1995, pp. 161–175.
doi:10.1117/12.208885

[21] Ruebsamen, D. T., Boyd, J., Vecera, J., and Nagel, R., "Development of a Dual Mode D-Strut Vibration Isolator for a Laser Communication Terminal," *Proceedings of the 38th Aerospace Mechanisms Symposium*, NASA Langley Research Center, Hampton, VA, May 2006, pp. 141–148.

[22] Richard, G. C., Jeanne, M. S., Alok, D., Davis, L. P., Hyde, T. T., Davis, T., Zahidul, H. R., and John, T. S., "Vibration Isolation and Suppression System for Precision System for Precision Payloads in Space," *Smart Materials and Structures*, Vol. 8, No. 6, 1999, pp. 798–812.
doi:10.1088/0964-1726/8/6/309

[23] Thayer, D., Campbell, M., Vagners, J., and von Flotow, A., "Six-Axis Vibration Isolation System Using Soft Actuators and Multiple Sensors," *Journal of Spacecraft and Rockets*, Vol. 39, No. 2, 2002, pp. 206–212.
doi:10.2514/2.3821

[24] Lee, D. O., Park, G., and Han, J. H., "Development of Vibration Isolation Platform for Low Amplitude Vibration," *Proceedings of the SPIE: Active and Passive Smart Structures and Integrated Systems*, Vol. 9057, SPIE, Bellingham, WA, March 2014, Paper 905708.
doi:10.1117/12.2044984

[25] Jiang, H. Z., He, J. F., and Tong, Z. Z., "Characteristics Analysis of Joint Space Inverse Mass Matrix for the Optimal Design of a 6-DOF Parallel Manipulator," *Mechanic and Machine Theory*, Vol. 45, No. 5, 2010, pp. 722–739.
doi:10.1016/j.mechmachtheory.2009.12.003

[26] Miller, D. W., Weck, O. L., and Mosier, G. E., "Framework for Multidisciplinary Integrated Modeling and Analysis of Space Telescopes," *Proceedings of the SPIE: Integrated Modeling of Telescopes*, Vol. 4757, SPIE, Bellingham, WA, 2002, pp. 1–18.
doi:10.1117/12.489831

[27] LoBosco, D. W., Blaurock, C., Chung, S., and Miller, D. W., "Integrated Modeling of Optical Performance for the Terrestrial Planet Finder Structurally Connected Interferometer," *Proceedings of the SPIE: Modeling and Systems Engineering for Astronomy*, Vol. 5497, SPIE, Bellingham, 2004, pp. 278–289.
doi:10.1117/12.550929

[28] Miller, D. W., de Weck, O. L., Uebelhart, S. A., Grogan, R., and Basdogan, I., "Integrated Dynamics and Controls Modeling for the Space Interferometry Mission (SIM)," *IEEE Proceedings of Aerospace Conference*, Vol. 4, IEEE, Piscataway, NJ, 2001, pp. 2089–2102.
doi:10.1109/AERO.2001.931545

[29] Knight, J. S., Acton, D. S., Lightsey, P., and Barto, A., "Integrated Telescope Model for the James Webb Space Telescope," *Proceedings of the SPIE: Modeling, Systems Engineering, and Project Management for Astronomy V*, Vol. 8449, SPIE, Bellingham, WA, 2012, Paper 84490V.
doi:10.1117/12.926814

[30] Johnston, J. D., Howard, J. M., Mosier, G. E., and Parrish, K. A., "Integrated Modeling Activities for the James Webb Space Telescope Structural-Thermal-Optical Analysis," *Proceedings of the SPIE: Optical, Infrared, and Millimeter Space Telescopes*, Vol. 5487, SPIE, Bellingham, WA, 2004, pp. 600–610.
doi:10.1117/12.551704

[31] Chen, C. R., Chen, C. W., and Yang, M. Y., "Integrated Analysis of FORMOSAT-5 Remote Sensing Instrument in Space," *Proceedings of the SPIE: Optical Modeling and Performance Predictions VI*, Vol. 8840, SPIE, Bellingham, 2013, Paper 88400K.
doi:10.1117/12.2021559

[32] McInroy, J. E., and Hamann, J., "Design and Control of Flexure Jointed Hexapods," *IEEE Transactions on Robotics and Automation*, Vol. 16, No. 4, Aug. 2000, pp. 372–381.
doi:10.1109/70.864229

[33] Oscar, R., and Héctor, R., "Some Results on Symmetric Circulant Matrices and on Symmetric Centrosymmetric Matrices," *Linear Algebra and Its Applications*, Vol. 392, Nov. 2004, pp. 211–233.
doi:10.1016/j.laa.2004.06.013

[34] Chen, Y. X., and McInroy, J. E., "Decoupled Control of Flexure-Jointed Hexapods Using Estimated Joint-Space Mass-Inertia Matrix," *IEEE Transactions on Control Systems Technology*, Vol. 12, No. 3, May 2004, pp. 413–421.
doi:10.1109/TCST.2004.824339

[35] Genberg, V., Doyle, K., and Michels, G., "Optical Performance as a Function Dynamic Mechanical Loading," *Proceedings of the SPIE: Optical Modeling and Performance Predictions*, Vol. 5178, SPIE, Bellingham, WA, Aug. 2003, pp. 14–19.
doi:10.1117/12.507859

[36] Doyle, K., Genberg, V., and Michels, G., *Integrated Optomechanical Analysis*, 1st ed., SPIE Publ., Bellingham, WA, Oct. 2002, pp. 127–144, Chap. 4.

[37] Agrawal, B., "Jitter Control for Imaging Spacecraft," *The 4th Recent Advances in Space Technologies International Conference*, IEEE, Piscataway, NJ, 2009, pp. 615–620.
doi:10.1109/RAST.2009.5158266